

Supplementary Information

Current-in-plane Tunneling Measurement of Oxygen-functionalized Few-layer Boron Nitride Lateral Barriers

Ziba Torkashvand^{a,b}, Kavos Mirabbaszadeh^{a,*}, Farzaneh Shayeganfar^{a,c}, Pawan Kumar Srivastava^b, Changgu Lee^b, Mohadese Beigtan^d

^a*Department of Physics and Energy Engineering, Amirkabir University of Technology, Tehran 15875-4413, Iran*

^b*School of Mechanical Engineering, Sungkyunkwan University, Suwon 16419, South Korea*

^c*Department of Aerospace Engineering, University of Michigan, Ann Arbor, MI 48109, USA*

^d*School of Advanced Materials Science & Engineering, Sungkyunkwan University, Suwon 16419, South Korea*

1. Effect of electrode composition

Nickel, based on the experimental growth process and DFT calculations, not only has an excellent work function alignment for charge injection but also has low lattice mismatch and the desired adsorption height on hBN[1, 2]. Hence, for the next step, we used the nickel/gold combination as the electrode materials along with a good performance of considering large area contacts to see the effect of the improvement of contacts on the level of tunneling current and noise in charge injection. Figures S1 (a) and (b) show our devices with large electrode contacts and different channel lengths (2 and 3 μm). Figure S1 (c) shows the $I_D - V_D$ graph for the devices shown in panels (a) and (b). This behavior shows that although the noise fluctuations decreased, there exists still a constant level of tunneling current in the bias range, regardless of the channel length. From the I-V curve, it can be seen that for the large contact area device the level of current leakage is lower than the small contact area devices.

2. Effect of annealing

Next, we proceed to examine two large hBN samples in order to make long-width (W) devices. For this purpose, we prepared (see Experimental section) two devices with channel widths of 50.33 and 73.04 μm and channel lengths (L) of 2 and 1 μm , as shown in Figure S2. Before electrical characterization, we annealed the devices for 10 min at 770 K in an Ar environment using rapid

*corresponding authors

Email addresses: mirabbas@aut.ac.ir (Kavos Mirabbaszadeh), fshayega@umich.edu (Farzaneh Shayeganfar)

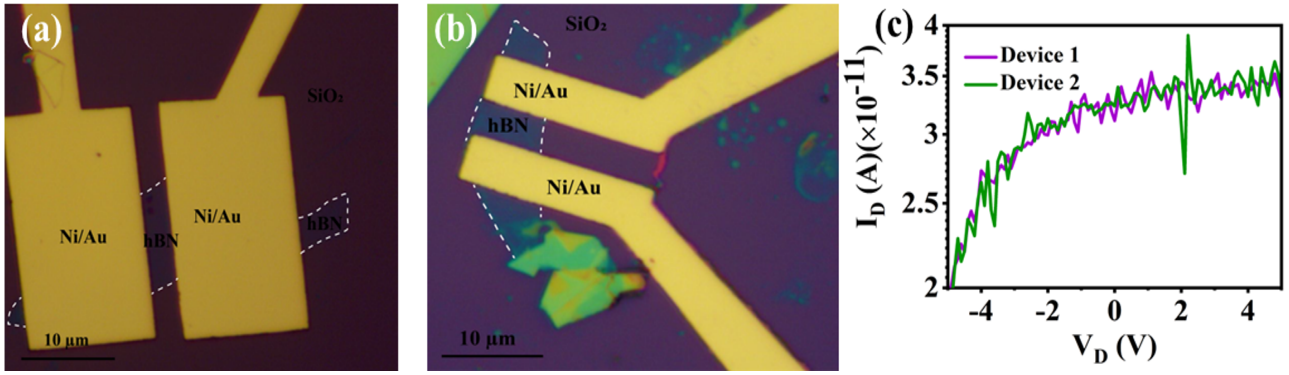


Fig. S1: Electrical characterization of large contact area with different channel-length hBN FETs. (a) Optical image of the fabricated hBN FET with large contact area and channel length equal to $2 \mu\text{m}$ (b) Optical image of the fabricated hBN FET with large contact area and channel length equal to $3 \mu\text{m}$ (c) $I_D - V_D$ graph for large contact devices in panels (a) and (b). From the I-V curve it can be seen that although the level of noise fluctuations decreased, there exists still a high level of resistant behavior, regardless of the channel length.

thermal annealing (RTA). As can be seen from Figures S2 (c) and (d), there is no change or damage in devices after high-temperature annealing. Figure S2 (e) shows the $I_D - V_G$ graph at $V_D = 1V$ for two long-channel devices shown in panels (c) and (d). From Figure S2 (e), one can see that device $73.04 \mu\text{m}$ shows a more robust level of fluctuations but in a higher level of tunneling currents, while this behavior is smoother for device $50.33 \mu\text{m}$, which may be because of the lack of proper contact in the device $73.04 \mu\text{m}$.

3. Electronic properties and mechanical stability

The relaxed structure of one to three-layer AA' stacking hBN is presented in figures S3 (a) to (c). We used DFT-PBE formalism for phonon calculations. The details are provided in the Experimental section. The phonon dispersion of considered few-layer hBN is provided in Figure S3 (d) to (f). For the three cases, a minimum of three acoustic branches are almost linear near the center of the Brillouin zone (Γ) point without any negative frequency. As it can be seen from phonon dispersion graphs, higher phonon modes up to 4500 Hz for hBN suggest the capability of hBN for use as the dielectric for high-temperature and high-electric-field devices rather than SiO_2 [3]. The calculated band structure for one to three layers of hBN is provided in Figures S3 (g) to (i). The direct bandgap of few-layer hBN increases as the number of layers decreases; hence monolayer hBN shows the largest bandgap of 4.64 eV at the K point in good agreement with previous reports [4, 5, 6].

The total density of states (TDOS) and the projected density of states (PDOS) graphs projected

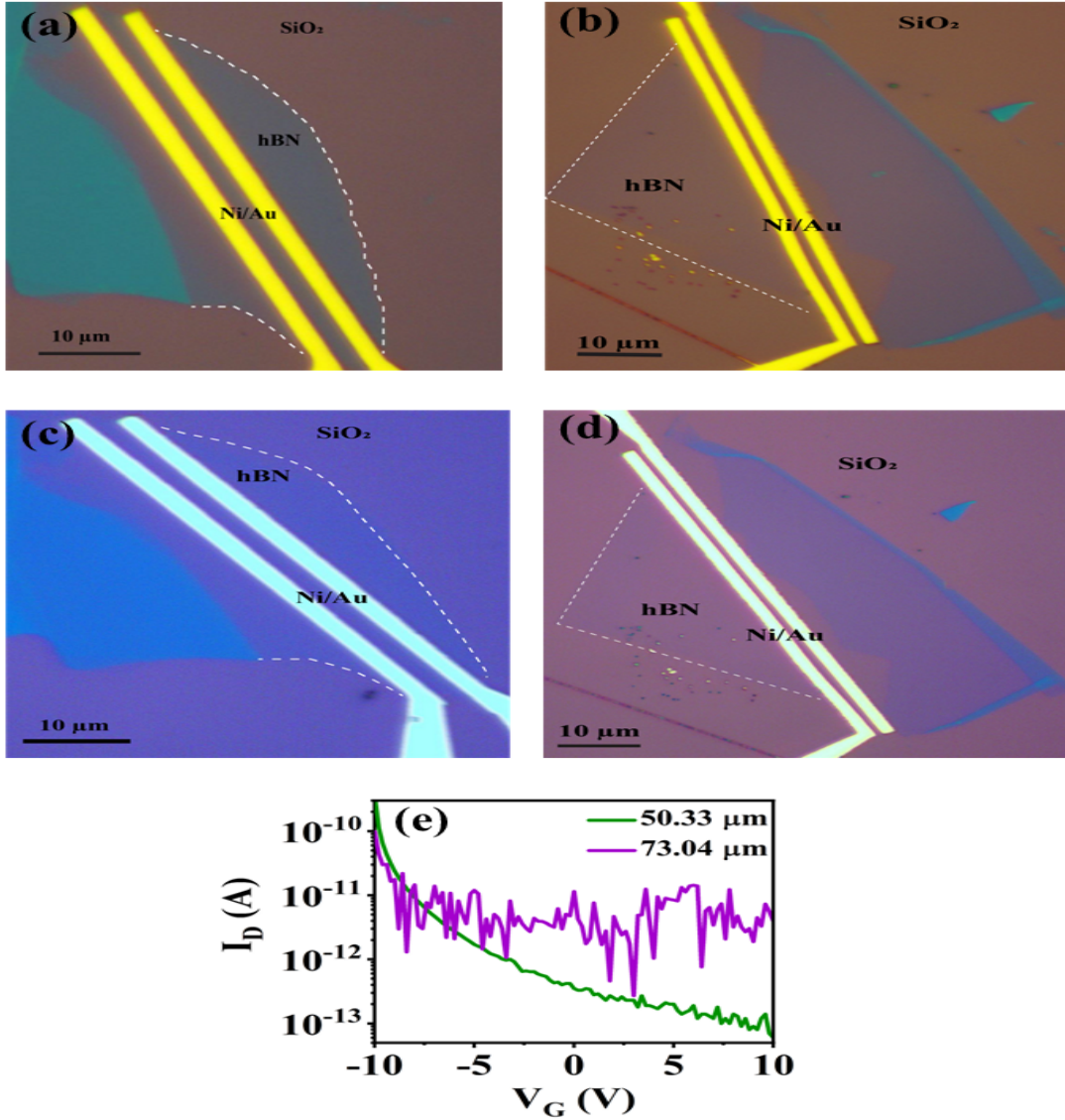


Fig. S2: Electrical characterization of hBN FET with long channel width after annealing. (a) Optical image of the fabricated hBN FET with channel width equal to $50.33 \mu\text{m}$ and channel length equal to $2 \mu\text{m}$ before annealing (b) Optical image of the fabricated hBN FET with channel width equal to $73.04 \mu\text{m}$ and channel length equal to $1 \mu\text{m}$ before annealing (c) Optical image of the device in (a) after annealing. (d) Optical image of the device in (b) after annealing. (e) $I_D - V_G$ graph at $V_D = 1V$ for the devices in (c) and (d). There is a strong level of fluctuation for the $I_D - V_G$ curve of device $73.04 \mu\text{m}$ which may be because of the lack of good contact.

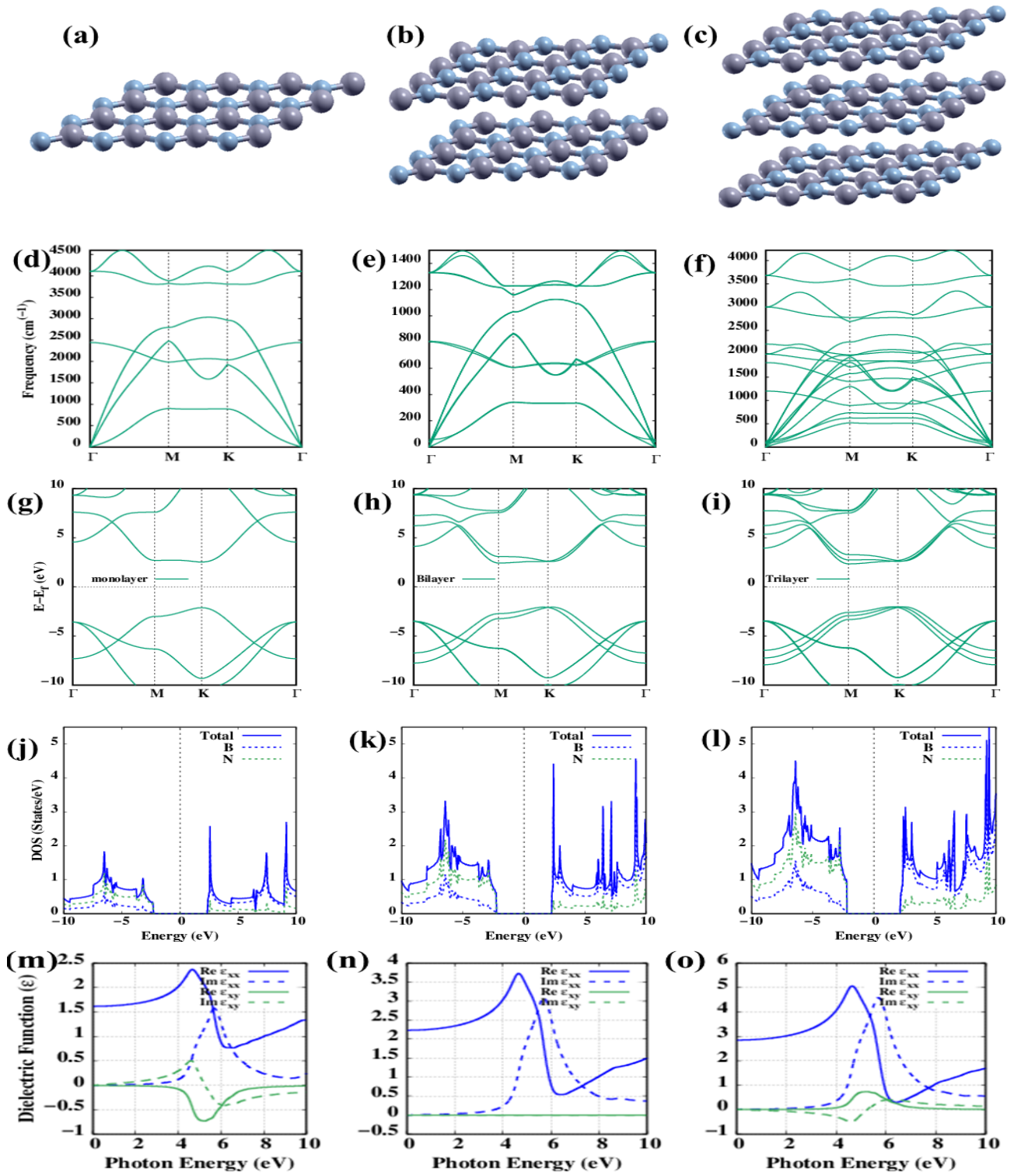


Fig. S3: (a) to (c) Fully relaxed pristine mono-, bi-, and trilayer hBN structures. (d) to (f) Phonon dispersion for pristine mono-, bi-, trilayer hBN structures. (g) to (i) The energy band structure of pristine mono-, bi-, trilayer hBN structures. The Fermi level is set to zero. (j) to (l) Corresponding TDOS (solid blue line) and PDOS (dashed blue and green lines) projected to the boron and nitrogen atoms, respectively. (m) to (o) Calculated real part (solid lines) and imaginary part (dashed lines) of both diagonal ϵ_{xx} (blue) and off-diagonal ϵ_{xy} (green) dielectric functions of mono-, bi-, and trilayer hBN structures.

on boron and nitrogen atoms corresponding to one to three-layer hBN are presented in figures S3 (j) to (l). The largest bandgap through these three considered cases is evident from the density of states, as well. The diagonal (ϵ_{xx}) and off-diagonal (ϵ_{xy}) parts of the dielectric function for the three hBN cases are shown in figures S3 (m) to (o). The imaginary part of the dielectric function (dashed blue lines) has its maximum at 5.68, 5.69, and 5.69 eV for the three cases, respectively. Interestingly, for bilayer hBN the off-diagonal parts of the real and imaginary dielectric function have zero value through the whole spectrum. Since the magneto-optical Kerr effects for materials are directly related to this value [7], it can be perceived as a sign of lack of Kerr capability of bilayer hBN however, it needs more verification. The layer-dependent dielectric constant is obviously ranging from 1.61 to 2.84, in good agreement with other layer-dependent reported values[8, 9]. Generally, what can be seen from the provided graphs is that the dielectric constant is in a trade-off with bandgap for the application in device fabrication.

In this context, we introduced one oxygen atom (nitrogen vacancy) to the 4×4 supercell of a hexagonal boron nitride sheet. Figures S4 (a) to (d) illustrate the relaxed structures of four oxygen-functionalized configurations, namely the bridge site (BR), nitrogen-vacancy (NV), oxygen-substitution (OS), and top boron (TB). Correspondingly, Figures S4 (e) to (h) present the calculated spin-polarized energy band structures, with solid blue and green lines indicating spin-up and spin-down, respectively, for the structures depicted in (a) to (d).

A notable observation is the reduction in the bandgap value from 4.64 eV for pristine hBN to 3.33 eV for BR. In the cases of BR and NV, bands originating from mid-gap states, induced by surface modifications, appear almost flat, resembling localized impurity states contributing to the conduction bands. Furthermore, for NV, there is a transformation in electronic nature from a wide bandgap semiconductor to a metal, a consequence of Fermi level band crossing.

In contrast, for OS and TB, the Fermi level intersects with the spin-up/down bands of conduction/valence bands, indicating a half-metallic behavior in these structures. This behavior aligns with prior reports on functionalized structures [10].

Figures S4 (i) to (l) depict the spin-polarized total density of states (TDOS) with solid blue and green lines representing spin up and down, respectively. Additionally, the projected density of states (PDOS) is illustrated with dashed blue and green lines, corresponding to spin up and down and projected onto the oxygen atoms.

For all four oxygen-functionalized hBN cases, there is a noticeable presence of excessive midgap states after oxygen functionalization, indicating a consistent electronic nature throughout the en-

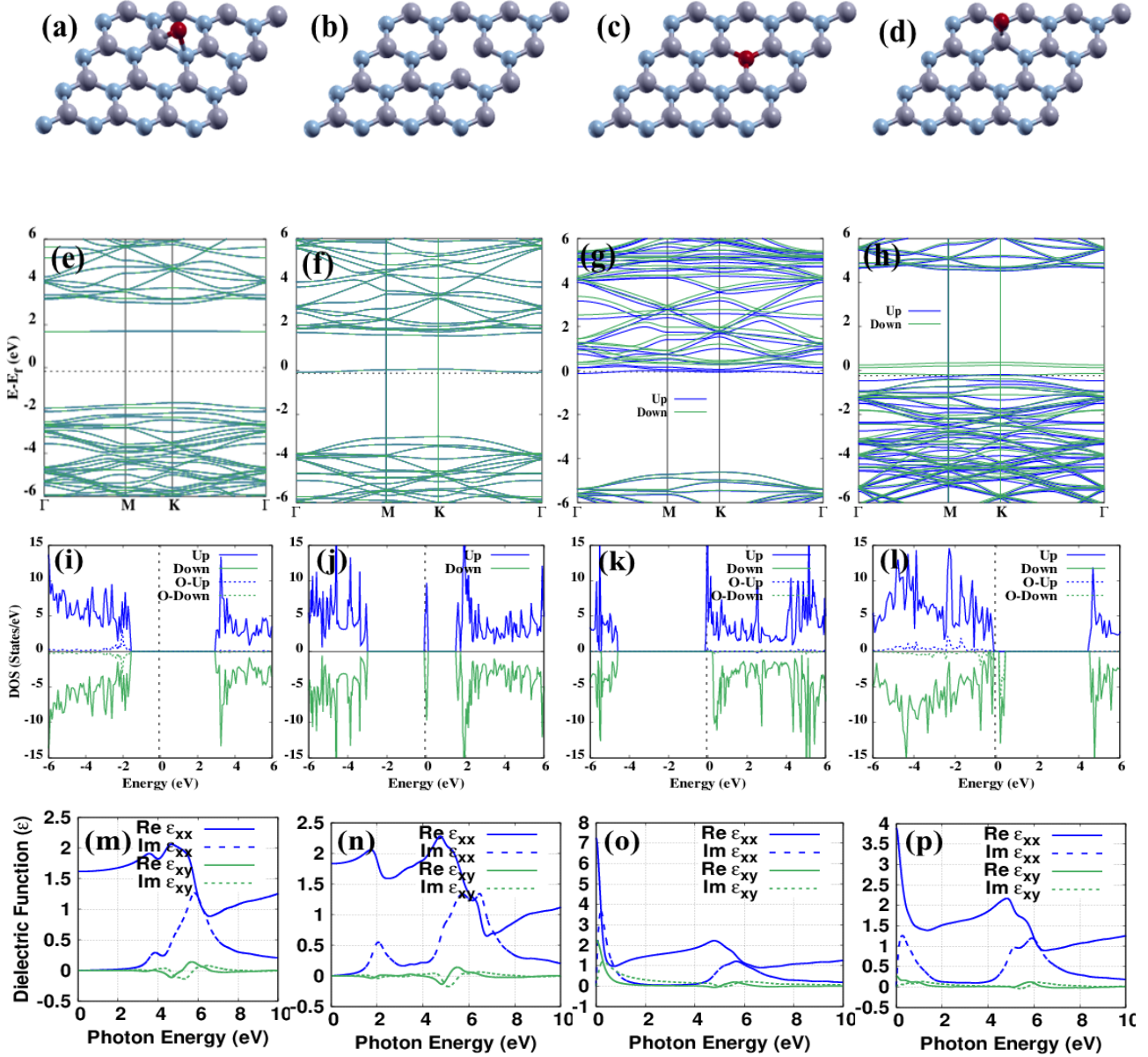


Fig. S4: (a) to (d) Fully relaxed four functionalized hBN structures, bridge site (BR), nitrogen-vacancy (NV), oxygen-substitution (OS), and top boron (TB). (e) to (h) The spin-polarized energy band structure for the structures in (a) to (d) (solid blue, green lines for spin up, down, respectively). (i) to (l) Corresponding TDOS (solid blue and green lines for spin up and down) and PDOS (dashed blue and green lines for the spin up and down) projected to the oxygen atoms, respectively for structures in (a) to (d). (m) to (p) Calculated real part (solid lines) and imaginary part (dashed lines) of both diagonal ϵ_{xx} (blue) and off-diagonal ϵ_{xy} (green) dielectric functions of the four functionalized hBN structures in (a) to (d).

ergy band structure. In Figure S4 (i), the DOS does not show an added electronic state due to the presence of the flat band introduced by the bridge-bonded oxygen. However, in Figure S4 (j), for the nitrogen vacancy case, the added state exhibits enough dispersion to manifest as an excessive electronic state in the DOS. Similar patterns of excessive states interfering with the Fermi level are observed for oxygen substitution and oxygen positioned on top of the boron atom, as depicted in Figures S4 (k) and (l).

Across all cases, B and N contribute equally to the valence band maximum (VBM) and conduction band minimum (CBM). Yet, in proximity to the Fermi level, the oxygen atoms dominate the contribution. Notably, in the case of NV, a distinct state near the Fermi level suggests its potential as a single-photon emitter.

The diagonal (ϵ_{xx}) and off-diagonal (ϵ_{xy}) parts of the dielectric function for the four types of oxygen-functionalized-hBN are shown in figures S4 (m) to (p). The imaginary part of the dielectric function (dashed blue lines) has its maximum at 5.82, 6.46, 5.67, and 5.91 eV for the four cases, respectively. Moreover, the off-diagonal part of the dielectric function, as evident in Figures S4 (m) to (p), illustrates that after oxidation, the peak intensity diminishes, resulting in a reduced Kerr capability. The dielectric behavior of materials is evident in the real and imaginary components of the dielectric function at low frequencies. Our findings indicate that hexagonal boron nitride (hBN) maintains a significant level of dielectricity even after surface modification. The dielectric constant from the diagonal part of the dielectric function exhibits an increase from 1.59 for pristine hBN to 1.61, 1.83, 7.25, and 3.89 for different surface functionalizations. This aligns well with the results observed in current-level measurements before and after plasma treatment, as illustrated in Figure 1 (d). The decrease in current levels after plasma treatment is attributed to the enhanced dielectric nature of hBN, facilitated by the introduction of oxygen atoms to the surface.

References

- [1] F. Mahvash, E. Paradis, D. Drouin, T. Szkopek, M. Siaj, Space-Charge Limited Transport in Large-Area Monolayer Hexagonal Boron Nitride, *Nano Letters* 15 (4) (2015) 2263–2268. [doi:10.1021/nl504197c](https://doi.org/10.1021/nl504197c).
- [2] W. Auwärter, [Hexagonal boron nitride monolayers on metal supports: Versatile templates for atoms, molecules and nanostructures](#), *Surface Science Reports* 74 (1) (2019) 1–95. [doi:](#)

[10.1016/j.surfrep.2018.10.001](https://doi.org/10.1016/j.surfrep.2018.10.001).

URL <https://doi.org/10.1016/j.surfrep.2018.10.001>

- [3] I. Meric, M. Y. Han, A. F. Young, B. Ozyilmaz, P. Kim, K. L. Shepard, Current saturation in zero-bandgap, top-gated graphene field-effect transistors, *Nature Nanotechnology* 3 (11) (2008) 654–659. [doi:10.1038/nnano.2008.268](https://doi.org/10.1038/nnano.2008.268).
- [4] J. Kang, L. Zhang, S. H. Wei, A Unified Understanding of the Thickness-Dependent Bandgap Transition in Hexagonal Two-Dimensional Semiconductors, *Journal of Physical Chemistry Letters* 7 (4) (2016) 597–602. [doi:10.1021/acs.jpcllett.5b02687](https://doi.org/10.1021/acs.jpcllett.5b02687).
- [5] D. Wickramaratne, L. Weston, C. G. Van De Walle, Monolayer to Bulk Properties of Hexagonal Boron Nitride, *Journal of Physical Chemistry C* 122 (44) (2018) 25524–25529. [doi:10.1021/acs.jpcc.8b09087](https://doi.org/10.1021/acs.jpcc.8b09087).
- [6] M. Topsakal, E. Aktürk, S. Ciraci, First-principles study of two- and one-dimensional honeycomb structures of boron nitride, *Physical Review B - Condensed Matter and Materials Physics* 79 (11) (2009) 115442. [doi:10.1103/PhysRevB.79.115442](https://doi.org/10.1103/PhysRevB.79.115442).
- [7] J. K. Butler, M. Martinez, R. Kilci, G. A. Evans, Optical Properties of Iron to 30 eV, *Materials Sciences and Applications* 12 (12) (2021) 622–638. [doi:10.4236/msa.2021.1212042](https://doi.org/10.4236/msa.2021.1212042).
- [8] F. Ferreira, A. J. Chaves, N. M. R. Peres, R. M. Ribeiro, Excitons in hexagonal boron nitride single-layer: a new platform for polaritonics in the ultraviolet, *Journal of the Optical Society of America B* 36 (3) (2019) 674. [doi:10.1364/josab.36.000674](https://doi.org/10.1364/josab.36.000674).
- [9] A. Laturia, M. L. Van de Put, W. G. Vandenberghe, Dielectric properties of hexagonal boron nitride and transition metal dichalcogenides: from monolayer to bulk, *npj 2D Materials and Applications* 2 (1). [doi:10.1038/s41699-018-0050-x](https://doi.org/10.1038/s41699-018-0050-x).
- [10] Q. Weng, D. G. Kvashnin, X. Wang, O. Cretu, Y. Yang, M. Zhou, C. Zhang, D. M. Tang, P. B. Sorokin, Y. Bando, D. Golberg, Tuning of the Optical, Electronic, and Magnetic Properties of Boron Nitride Nanosheets with Oxygen Doping and Functionalization, *Advanced Materials* 29 (28) (2017) 1700695. [doi:10.1002/adma.201700695](https://doi.org/10.1002/adma.201700695).